Geophysical Journal International

Geophys. J. Int. (2018) **213,** 1113–1120
Advance Access publication 2018 February 5
GJI Seismology

doi: 10.1093/gji/ggy049

The 2014, M_W6.9 North Aegean earthquake: seismic and geodetic evidence for coseismic slip on persistent asperities

Ali Ozgun Konca,[1] Seda Cetin,[2] Hayrullah Karabulut,[1,3] Robert Reilinger,[4] Ugur Dogan,[2] Semih Ergintav,[5] Ziyadin Cakir[6] and Ergin Tari[7]

[1] *Department of Geophysics, Kandilli Observatory and Earthquake Research Institute, Bogazici University,* 34684 *Istanbul, Turkey.*
E-mail: ozgun.konca@boun.edu.tr
[2] *Department of Geomatics, Yildiz Technical University,* 34220 *Istanbul, Turkey*
[3] *EOST, CNRS/Universite de Strasbourg, F-*67084 *Strasbourg, France*
[4] *Department of Earth, Atmospheric and Planetary Sciences, Massachusetts Institute of Technology, Cambridge,* 02139 *MA, USA*
[5] *Department of Geodesy, Kandilli Observatory and Earthquake Research Institute, Bogazici University,* 34684 *Istanbul, Turkey*
[6] *Department of Geology, Istanbul Technical University,* 34469 *Istanbul, Turkey*
[7] *Department of Geomatics, Istanbul Technical University,* 34469 *Istanbul, Turkey*

Accepted 2018 February 4. Received 2018 January 18; in original form 2017 July 5

SUMMARY

We report that asperities with the highest coseismic slip in the 2014 M_W6.9 North Aegean earthquake persisted through the interseismic, coseismic and immediate post-seismic periods. We use GPS and seismic data to obtain the source model of the 2014 earthquake, which is located on the western extension of the North Anatolian Fault (NAF). The earthquake ruptured a bilateral, 90 km strike-slip fault with three slip patches: one asperity located west of the hypocentre and two to the east with a rupture duration of 40 s. Relocated pre-earthquake seismicity and aftershocks show that zones with significant coseismic slip were relatively quiet during both the 7 yr of interseismic and the 3-month aftershock periods, while the surrounding regions generated significant seismicity during both the interseismic and post-seismic periods. We interpret the unusually long fault length and source duration, and distribution of pre- and post-main-shock seismicity as evidence for a rupture of asperities that persisted through strain accumulation and coseismic strain release in a partially coupled fault zone. We further suggest that the association of seismicity with fault creep may characterize the adjacent Izmit, Marmara Sea and Saros segments of the NAF. Similar behaviour has been reported for sections of the San Andreas Fault, and some large subduction zones, suggesting that the association of seismicity with creeping fault segments and rapid relocking of asperities may characterize many large earthquake faults.

Key words: Seismic cycle; Earthquake source observations; Seismicity and tectonics.

1 INTRODUCTION

Improvements in the spatial coverage and precision of seismic and geodetic observations are allowing identification of variations in coseismic slip for large earthquakes, and hence are providing constraints on the role of asperities and aseismic slip in the earthquake cycle (e.g. Aki 1984). The extent to which asperities persist through multiple earthquake cycles remains an area of research, and may well vary for different faults, but at least some studies interpret seismic activity as evidence for persistent asperities on subduction plate interfaces (e.g. Yamanaka & Kikuchi 2004 and references therein; Yue *et al.* 2013; Métois *et al.* 2016; Frank *et al.* 2017), as well as for continental strike-slip faults, including the San Andreas (e.g. Shirzaei & Bürgmann 2013; Jolivet *et al.* 2015) and North Anatolian faults (Bohnhoff *et al.* 2013; Ergintav *et al.* 2014; Schmittbuhl *et al.* 2015). These studies highlight the association of seismicity with areas of fault creep, and the role of fault creep and asperities in controlling the magnitude, initiation, propagation, and the strong ground motion of large earthquakes, critical parameters for earthquake hazard assessment.

A case in point, and the subject of this study, is the 2014 May 24 M_w6.9 North Aegean earthquake (Saltogianni *et al.* 2015) that occurred at the western continuation of the northern branch of the North Anatolian Fault (NAF) beneath the North Aegean Sea Trough (NAST; Fig. 1). The NAF is a >1200 km long continental strike-slip fault that accommodates the westward motion and counter-clockwise rotation of the Anatolian region with respect to Eurasia at rates of ~25 mm yr^{-1} (Reilinger *et al.* 2006; Vernant *et al.* 2014).

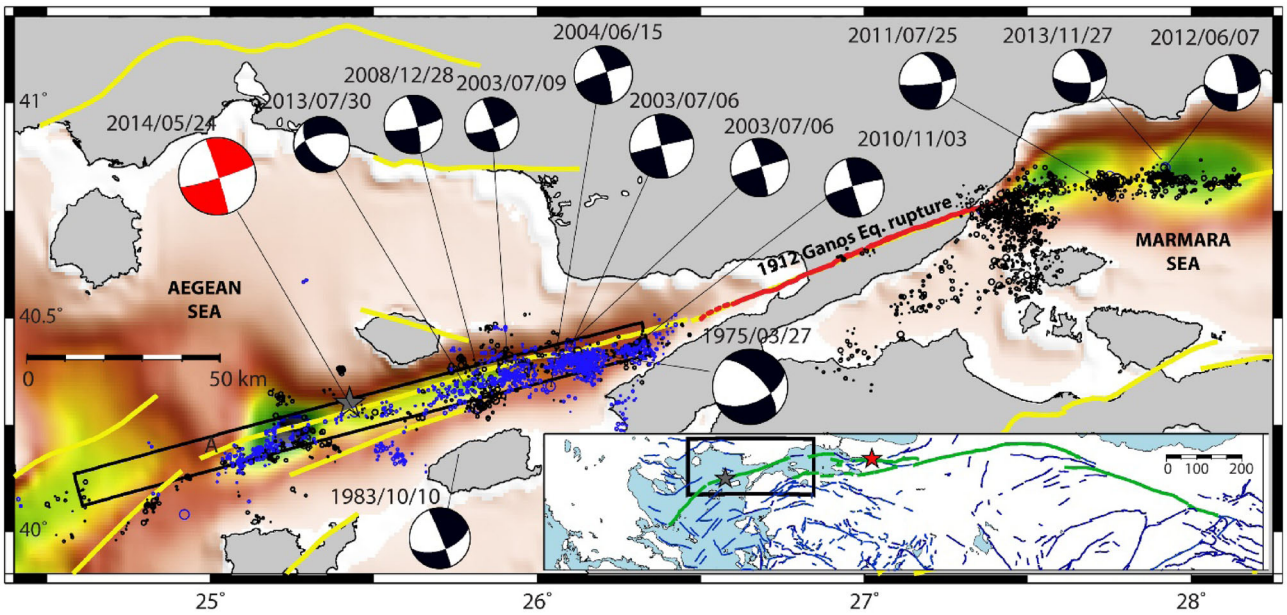

Figure 1. Seismotectonic map of the northeastern Aegean and western Marmara Sea region. Thick yellow lines are active faults (Emre *et al.* 2013). Red trace shows the estimated surface break of the 1912 Ganos earthquake (Aksoy *et al.* 2010). Seismic activity before the 2014 North Aegean earthquake (2007 January 1 to 2014 May 24) is shown by black circles and aftershocks are shown by blue circles. The focal mechanisms of significant earthquakes ($M_W \geq 4.7$) since 1975 are also shown by black beach balls from Global CMT and other studies (Taymaz *et al.* 1991; Karabulut *et al.* 2006). Red beach ball represents the mechanism of 2014 M_w6.9 North Aegean earthquake from Global CMT catalogue. The black box shows the outside edges of the finite-fault used in this study. Inset: the study area (shown by black rectangle) on a regional map covering North Anatolia, Aegean Sea and Greece. The NAFZ is shown by the green line and the epicentres of 2014 North Aegean and 1999 Izmit earthquakes are shown by grey and red stars, respectively.

The NAF failed in a sequence of $M > 7$ earthquakes during the 20th Century (Stein *et al.* 1997), the most recent being the 1999, M_W7.5, Izmit earthquake. In the Marmara region of northwestern Turkey, the fault bifurcates. The main branch follows the north shore of the Marmara Sea, traverses the Ganos Peninsula to Saros Bay, and connects with the offshore, transtensional basins that form the NAST system (Fig. 1). Only the segment of the NAF beneath the Sea of Marmara remains unbroken by a major 20th century earthquake (e.g. Armijo *et al.* 2005); prior earthquakes on this segment remain the subject of debate, but apparently it has not broken in a major earthquake since 1766 and perhaps even longer (e.g. Ambraseys 2002), suggesting the possibility of major earthquakes on this segment in the near future (Parsons 2004).

However, the amount of coupling beneath the Marmara has itself been a subject of debate (e.g. Meade *et al.* 2002); there is growing geodetic and seismic evidence that the Marmara segment is made up of zones that are coupled separated by segments that are partially or fully unlocked, suggesting the possibility the seismic gap might be filled by smaller future earthquakes (Ergintav *et al.* 2014; Schmittbuhl *et al.* 2015; Klein *et al.* 2017), a view not inconsistent with interpretations of seismicity beneath Marmara Sea during the last 500 yr (Ambraseys & Jackson 2000).

In this paper, we use seismic and GPS observations bracketing the 2014 North Aegean earthquake to investigate the character of the earthquake rupture, and the distribution of coseismic slip on the earthquake fault. From relocated hypocentres, we demonstrate that pre-earthquake seismicity, and aftershocks were pre-dominantly located around the periphery of fault patches with large coseismic slip. We attribute these observations to fault creep at the boundaries of locked asperities during strain accumulation; with the asperities relocking rapidly following the earthquake.

2 DATA, METHODS AND RESULTS

2.1 Relocated pre-earthquake seismicity and aftershocks

We relocated the background seismicity (between 2007 and 2014 before the main shock) and the aftershocks during the first 3 months following the main shock using the catalogues of two Turkish and one Greek agencies: General Directorate of Disaster Affairs of Turkey (AFAD), Bogazici University, Regional Earthquake-Tsunami Monitoring Center (BDTIM) and National Observatory of Athens (NOA) (see Supporting Information Fig. S1 for the station distribution map). For each event, the phase readings from all three catalogues were merged. The final catalogue of background seismicity contains more than 2700 events while the catalogue of aftershocks contains more than 1250 events (available by request).

In order to improve the hypocentre locations, we computed a 1-D velocity model using the VELEST inversion code (Kissling *et al.* 1994). Appropriate station corrections were applied for deviations from the 1-D velocity model. The average location errors for the background seismicity and aftershocks are described in Section S1 and shown in Figs S2 and S3, respectively, in the Supporting Information.

The earthquake locations were further improved using a double-difference relative location algorithm (Waldhauser & Ellsworth 2000; Waldhauser 2001). The relative location errors after the double-difference relocation are on the order of a few hundred metres (Supporting Information Fig. S4).

The map view of pre-2014 earthquake seismicity and aftershocks during the first three months following the main shock is shown in Fig. 1. The aftershocks are aligned along the NAST fault system quite linearly for about 120 km. There are also some secondary features at the eastern end of the fault and near the northwest tip of Gokçeada Island.

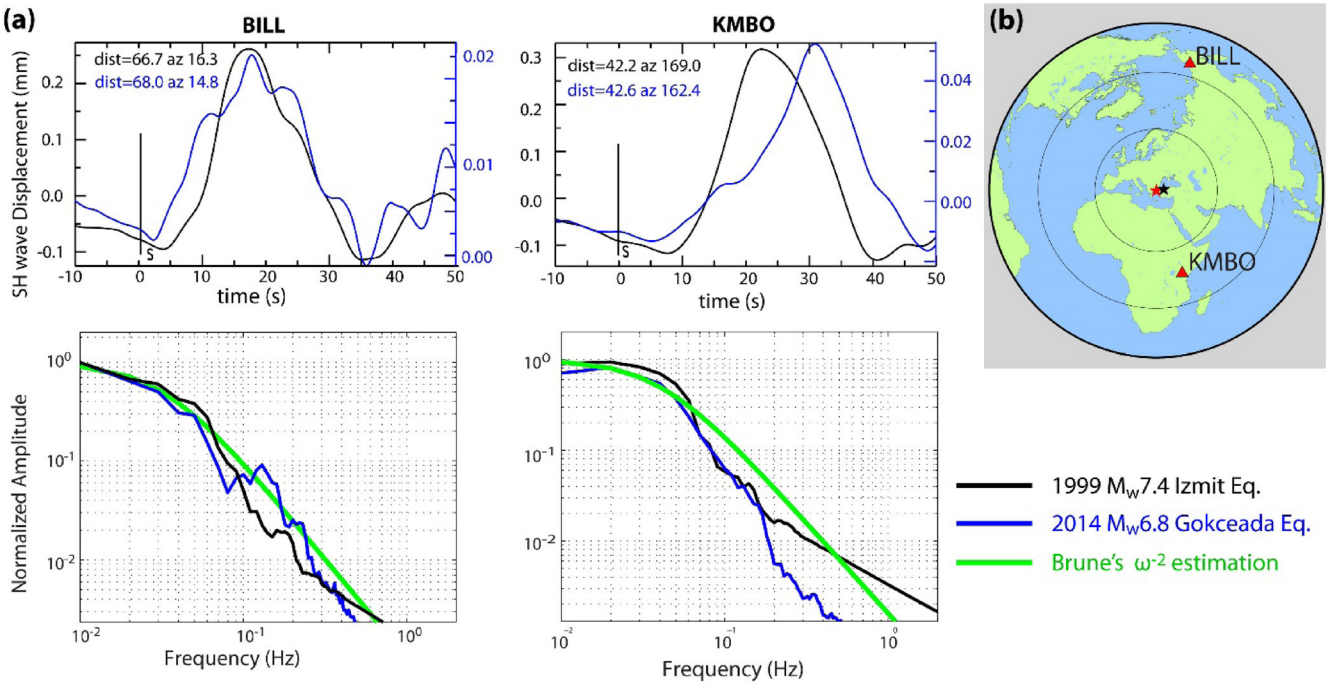

Figure 2. (a) Top: comparison of *SH* displacement waveforms recorded during the 1999 M_W7.5 Izmit (black) and 2014 M_W6.9 North Aegean (blue) earthquakes recorded at stations BILL and KMBO. Bottom: normalized spectra of the displacement waveforms and estimated spectra using ω^{-2} decay with corner frequency of 0.2 Hz for BILL and 0.25 Hz for KMBO stations. (b) The station locations (red triangles) and the locations of 1999 Izmit (black star) and 2014 North Aegean earthquakes (red star).

2.2 Long source duration and low stress drop

Comparison of teleseismic *SH* waves from the 2014 earthquake with those from the 1999 M_W7.5 Izmit earthquake (Fig. 2) shows that, despite one order of magnitude smaller moment of the 2014 event, it has a similar duration to the 1999 Izmit earthquake. The unusually long duration might be due to a slower rupture velocity, longer slip durations (rise times) and/or longer than expected fault rupture extent. In comparison, M_W7.1 Düzce earthquake, which occurred just to the east of 1999 Izmit earthquake three months later, had a source duration of 10 s and a bilateral rupture length of about 50 km (Konca *et al.* 2010). The 120 km length, and linear character of the aftershocks (Fig. 1) is good evidence for a longer than expected total rupture length for a typical M_W6.9 earthquake (Wells & Coppersmith 1994).

The spectra of the *S*-wave displacements show that the corner frequency of the 2014 event is comparable to that of the Izmit earthquake (Fig. 2). By comparing the far-field spectra at the BILL and KMBO stations with the Brune (1970) model of ω^{-2} decay, we estimate average corner frequencies of 0.2 and 0.25 Hz for BILL and KMBO, respectively (Fig. 2). Considering the linear relationship between seismic moment and stress drop (Brune 1970), and assuming similar corner frequencies for both events, the ratio of the stress drops of the M_W6.9 North Aegean earthquake to that of the 1999 M_W7.5 Izmit earthquake is about 1/10.

2.3 GPS data and coseismic displacements

We used GPS displacement data from 34 GPS stations, including 21 continuous stations and 5 survey sites in addition to displacement data from 8 stations in Greece reported by Saltogianni *et al.* (2015). GPS data were processed using the GAMIT/GLOBK software package (Herring *et al.* 2015) following standard procedures described in Reilinger *et al.* (2006). Supporting Information Table S1 lists details of the GPS observations and coseismic displacements, and Fig. 3 shows estimated coseismic offsets for the 34 GPS stations and survey sites used in this study. Procedures for continuously recording and survey sites which were part of this study are explained in the Supporting Information (Section S2) and the daily time-series for four stations are shown in Supporting Information Fig. S5.

2.4 Coseismic slip distribution and temporal behaviour of the 2014 earthquake

To estimate the distribution of slip on the coseismic fault, we used the finite-fault model program of Ji *et al.* (2002), which uses a simulated annealing algorithm to find the best-fitting slip model, variable rupture velocity, and rise time duration by the joint modelling of seismic and geodetic data. We used a single fault plane with strike angle of 75° and dip angle of 75° based on the lateral and depth distribution of seismicity (Fig. 1). The information on the teleseismic data and finite-fault modelling parameters are given in the Supporting Information (Section S3).

Fig. 4(a) shows the slip distributions obtained from the GPS data only and joint inversion of GPS and seismic data; comparison between observed and modelled coseismic displacements is shown in Fig. 3 for the joint inversion. The two solutions are quite similar showing that the slip distribution is primarily constrained by the GPS data.

The joint slip model shows multiple slip patches that extend from 25 km west to 65 km east of the hypocentre. The large slip patch ruptured towards the west from the hypocentre, and the two smaller patches ruptured towards east. The larger, western asperity extends to greater depths compared to the asperities east of the hypocentre.

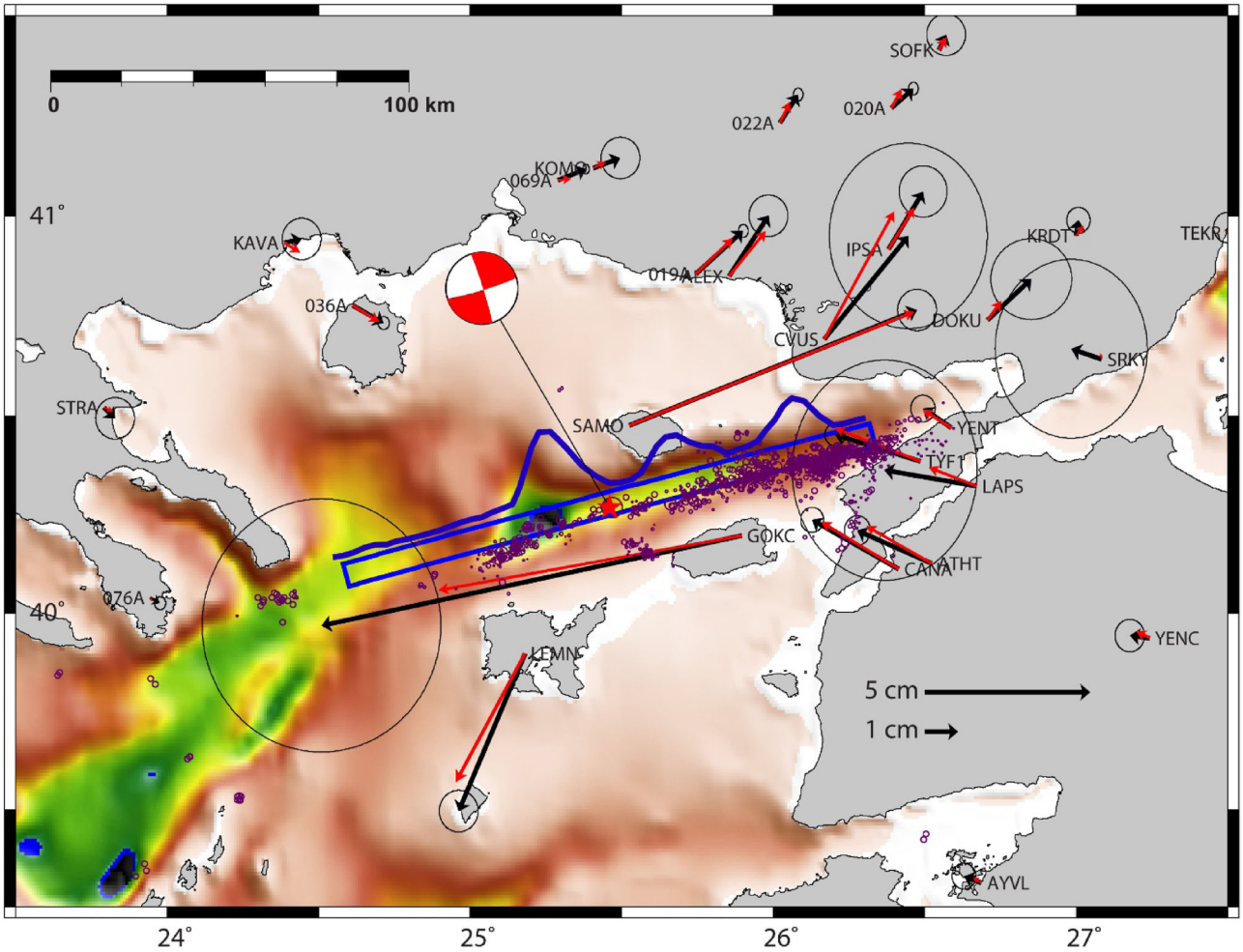

Figure 3. Coseismic offsets (black vectors) with 1σ error ellipses estimated for 34 GPS sites bracketing the 2014 earthquake (tabulated in Supporting Information Table S1). Red vectors show the horizontal displacements predicted from the joint slip model shown in Fig. 4(a). The map view of depth-averaged slip is shown by the blue curve. The blue rectangle shows the surface projection of the finite-fault model. The purple circles are the aftershocks. The star shows the hypocentre location.

The fits to the seismic data (Supporting Information Fig. S6) are satisfactory (Variance Reduction: 45.4 per cent for *P* and 55.2 per cent for *SH* waves). The quality of fits to the teleseismic data might imply a further complexity in the fault geometry which we were not able to constrain.

The fits to the GPS displacement vectors are quite good with most model predictions between 1σ ellipses (reduced chi squared of 1.2, Fig. 3); however, the displacement vectors are systematically under-predicted by our joint slip model including the far–field stations; which implies that GPS data requires more seismic moment. In order to regularize the underdetermined problem of finding the slip distribution on the fault plane, we constrain the seismic moment using the value from the Global CMT catalogue (Dziewonski *et al.* 1989; Ekstrom *et al.* 2012) during the inversion process. Considering that some of the GPS data have been collected in campaign surveys and the continuous station offsets are determined from the average of daily solutions (Supporting Information Fig. S5), we conclude that the underestimation of displacement vectors is due to early post-seismic slip.

In order to test the reliability of our slip model, we performed two resolution tests. Since our slip model primarily relies on the GPS data, we only included the GPS data. Test 1 is a checkerboard test, and Test 2 is based on the preliminary model of the 2014 earthquake. For each test model, we calculated the synthetic GPS displacements at the observation sites and added random error based on their measured uncertainties (see Supporting Information Section S4 and Fig. S6 for details).

In addition to resolution tests, we performed further tests to examine whether the patchy slip distribution we observe is robust or not. For this purpose, we tried an inverse model, where we increase the weight on the smoothness by 1 order of magnitude where we still observe similar patchiness in slip distribution with slightly higher errors due to over smoothing (Supporting Information Fig. S8b). We also performed numerous forward models using smoother slip, which show that the patchiness we observe is a robust feature with the given data set and constraints (Supporting Information Figs S8c–e). These tests are explained in detail in Supporting Information Section S4.

Based on the resolution tests, and other smoothness tests performed, we conclude that despite lack of sufficient near source data, the GPS and teleseismic observations, along with the constraint on seismic moment are sufficient to resolve the coseismic slip patches down to 15 km of the fault zone; however, some smearing of the actual slip is expected.

The average rupture velocity obtained from the finite-fault inversion is about 1.5–2 km s^{-1}. Due to the limited resolution of

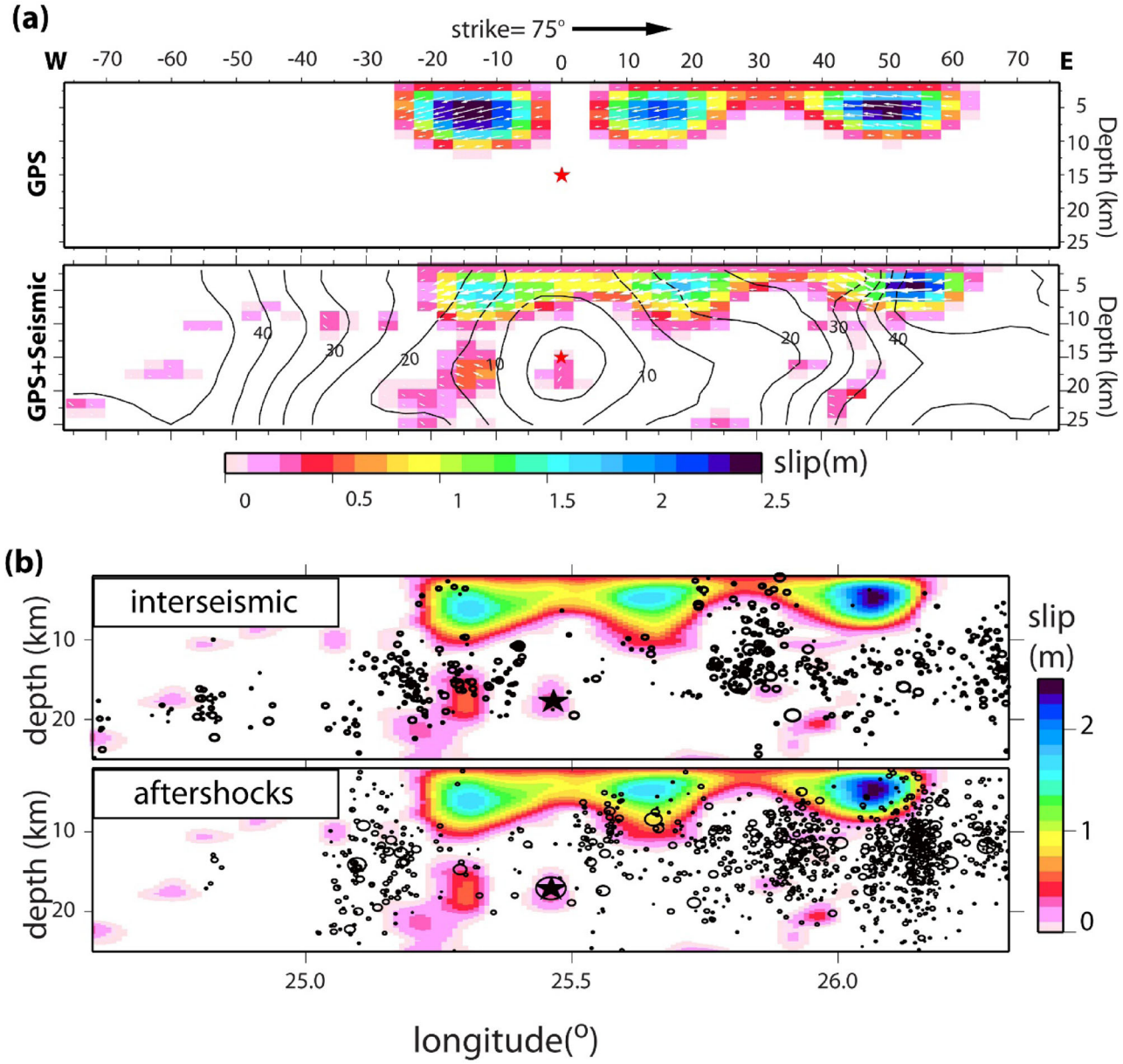

Figure 4. (a) Top: slip distribution obtained from modelling of GPS data. Bottom: slip distribution obtained from GPS and seismic data. The contours show the rupture front at 5 s intervals. Red star represents the hypocentre. (b) Top: coseismic slip distribution of the 2014 North Aegean earthquake and the seismicity before the main shock (2007 January 1 to 2014 May 24) projected onto the fault plane. Earthquakes are shown by black circles scaled by event magnitude. Bottom: the same as the top figure, showing the aftershocks (2014 May 24–August 1). Black star represents the hypocentre location.

fits to the seismic data in general, it is challenging to infer the rupture velocity accurately. However, considering the source duration of 35 s or longer (Saltogianni *et al.* 2015), and a unilateral rupture length of 60 km towards east, and assuming that the pulse duration is primarily due to rupture propagation, would yield an average rupture velocity of 1.5–2 km s^{-1}. Using back-projection of strong-motion data, Evangelidis (2015) inferred that the rupture propagated with a supershear rupture velocity (∼5.5 km s^{-1}) towards the east; much higher than the value obtained in this study. A characteristic of the supershear segments is that the main-shock fault plane is relatively silent while most of the aftershocks are off the main fault (Bouchon & Karabulut 2008). In the case of North Aegean earthquake, for most of the aftershocks east of the hypocentre, the distance to the fault plane is within the location error. Considering the pattern of seismicity along with the patchiness of slip distribution and the unusually long pulse duration of the earthquake, we infer that the rupture velocity is likely to be subshear.

The rupture length of the 1999 M_W7.5 Izmit earthquake is about 150 km (e.g. Delouis *et al.* 2002; Cakir *et al.* 2003) with the rupture velocity higher than the *S*-wave speed (Bouchon *et al.* 2001). The rupture length associated with the 1999 M_W7.1 Duzce earthquake is about 50 km and the source duration is about 10 s, again with a supershear rupture velocity (Konca *et al.* 2010). Considering the rupture length, unusually long source duration, and possibly slower rupture velocity, we conclude that the M_W6.9 2014 North Aegean event is not similar to the high rupture-speed, impulsive 1999 Izmit and Duzce earthquakes.

3 DISCUSSION

The observations show that the 2014 North Aegean earthquake had a patchy slip distribution with longer than expected rupture length, long rupture duration and complex source-time function, and low stress drop. It is clear that the stress was heterogeneous so that these asperities did not cooperate to generate a large impulsive earthquake.

We consider two explanations for the heterogeneous seismic and geodetic character of the 2014 earthquake. One possibility is that the fault was fully coupled, but only ruptured partially during the 2014 earthquake because of the heterogeneous stress distribution due to prior earthquakes (Konca *et al.* 2008; Yue *et al.* 2013). Alternatively, the fault was strongly coupled only where large coseismic slip occurred (asperities), and failed by fault creep between these locked patches during the interseismic period. In this case, the 2014 distribution of coseismic slip is an example of asperities that ruptured and the weakly coupled zones that did not rupture seismically during the earthquake.

Fig. 4(b) shows the joint slip model with seismicity before and after the 2014 earthquake projected on to the fault plane. Seismicity before the earthquake (Fig. 4b top panel) shows that the patches that ruptured during the 2014 event were relatively silent during the 7 yr of the interseismic period leading up to the earthquake. On the other hand, during these 7 yr, the surrounding regions that did not slip significantly during the earthquake generated most of the seismicity. This is consistent with asperities producing little seismicity while fully or partially creeping areas on the fault surface produce more small earthquakes during the interseismic period (e.g. Bohnhoff *et al.* 2013; Schmittbuhl *et al.* 2015; Harris 2017). In addition, the aftershocks of the 2014 event are also preferentially located in zones that did not rupture co-seismically (Fig. 4b, bottom panel). For the most part, aftershocks tend to surround the major slip patches, suggesting that post-seismic slip occurs preferentially around the edges of coseismic slip patches where stresses were induced by the earthquake. In addition, the time evolution of spatial distribution of aftershocks shows that the first few hours of aftershocks are right below the co-seismic rupture, while the seismicity then propagates further along the fault plane both horizontally and vertically during the first few days; implying that the aftershock distribution is possibly mimicking the post-seismic slip (Supporting Information Fig. S8) similar to the observations of 1999 Landers earthquake (Perfettini & Avouac 2007).

These relationships between coseismic slip, seismicity during interseismic period and aftershocks, strongly support the notion that the 2014 coseismic fault is characterized by locked asperities separated by zones of partial or full fault creep, and that the asperities relocked very quickly after the main shock.

The notion that seismicity during the interseismic period is primarily confined to creeping areas of the fault surface finds support from several seismic and geodetic studies of the western NAF, as well as other strike slip faults (Nadeau *et al.* 1995; Dreger *et al.* 2007; Harris 2017) as well as subduction zones.

For example, 2015 M_w8.3 Illapel earthquake broke a 150 km section of the Chilean subduction (Ruiz *et al.* 2016). This earthquake slip zone was surrounded by a weakly coupled zone that created significant seismicity during the 20 yr of interseismic period (Poli *et al.* 2017).

The Ganos segment of the NAF, which is known to be locked from geodetic studies (Ergintav *et al.* 2014) and previously ruptured during the M_W7.4, 1912 Ganos earthquake (Aksoy *et al.* 2010), has been relatively quiet seismically during the period 1975–2015 (Fig. 1). The situation is more complex beneath the Marmara Sea, where there is evidence for seismically quiet locked zones with little apparent seismicity separated by zones of weak coupling and significant seismicity and repeating earthquakes (Ergintav *et al.* 2014; Schmittbuhl *et al.* 2015; Schmittbuhl *et al.* 2016; Klein *et al.* 2017). The Princes' Islands segment in the eastern Marmara is also accumulating strain (Diao *et al.* 2016) and has little seismicity in the upper 10 km of the crust (Bohnhoff *et al.* 2013), again consistent with seismicity being located below the locked part of the fault. In these cases, the pattern of locking from geodesy is consistent with the seismicity distribution. Similarly, the 1999 Izmit and Duzce earthquakes had the largest coseismic offsets above $\sim$ 10 km (e.g. Delouis *et al.* 2002) where the faults had little seismicity before the main shocks, and fewer aftershocks on the main coseismic faults (Bohnhoff *et al.* 2016). The fault relocked after the 1999 earthquake, except the shallowest portion (Cakir *et al.* 2012; Hussain *et al.* 2016), and shows little seismicity on the seismogenic depth range of the main fault (Bohnhoff *et al.* 2016).

The Marmara and Ganos studies, the results presented here for the North Aegean earthquake, and seismic and geodetic studies of the San Andreas Fault (Waldhauser & Ellsworth 2002; Evans *et al.* 2012) support the interpretation that seismicity on the fault surface is primarily confined to creeping areas of the fault surface, at least on some sections of these continental strike-slip faults. In addition, geodetic and seismic studies of some large subduction earthquakes report that aftershocks are mostly confined to regions between asperities (e.g. Miyazaki *et al.* 2004; Yamanaka & Kikuchi 2004; Yue *et al.* 2013; Frank *et al.* 2017; Poli *et al.* 2017) suggesting that persistent asperities and intervening seismicity and aftershocks may be characteristic of the mechanics of many large earthquake faults.

Identifying seismicity with fault creep is important for refining earthquake forecasting, including estimates of earthquake magnitudes, and the locations where future earthquakes are most likely to rupture with the largest slip. For example, the apparent earthquake gap along the Main Marmara Fault has been reported to be capable of generating one or more $M > 7$ earthquakes based on the length of the seismic gap and the time since the previous earthquake estimated to have occurred on this fault segment (Hubert-Ferrari *et al.* 2000; Armijo *et al.* 2005). To the extent that the fault surface is characterized by both locked and creeping segments (Ergintav *et al.* 2014; Schmittbuhl *et al.* 2015), we would anticipate smaller events due to the reduction in accumulated strain, and hence less seismic slip than for a fully coupled fault zone. Furthermore, because it is very difficult to identify asperities from geodetic measurements during the strain accumulation process (Evans *et al.* 2012; Shirzaei & Bürgmann 2013), locating asperities seismically offers opportunities to estimate the locations on the fault where earthquakes are most likely to initiate, thereby helping to focus studies of earthquake initiation processes.

4 CONCLUSION

We use GPS and teleseismic observations to estimate the distribution of coseismic slip on the strike-slip fault that caused the 2014 M_W6.9 North Aegean earthquake. We use relocated seismicity during the 7 yr prior to the 2014 earthquake, and 3 months of aftershocks to investigate the relationship between patches of large coseismic slip (asperities) and hypocentral locations. Both pre-earthquake seismicity and aftershocks are mostly confined to areas on the fault surrounding the slip patches. Based primarily on these

observations, and the longer than expected fault length (from aftershocks) and earthquake duration, we conclude that the areas of large coseismic slip represent asperities that persisted through the period of strain accumulation and release for the 2014 event. The identification of background seismicity with creeping segments of the North Aegean coseismic fault, and the similar association of seismicity and fault creep on the adjacent western segment of the NAF (including the 1912 Ganos earthquake, Marmara Sea, and Princes Islands segments), support the notion that background seismicity provides information on the spatial distribution of fault coupling, important for estimating seismic hazards.

ACKNOWLEDGEMENTS

Pre-earthquake GPS surveys were supported by TÜBİTAK YDABAG (Project no: 103Y033) and İTÜ BAP (Project no: 30548) projects. MIT participation was supported in part by NSF Grant EAR-1622560. HK was supported by USIAS SEISNAF grant during his contribution to this work. We would like to thank two reviewers, Piero Poli and Romain Jolivet, for helpful comments on our original submission. We are grateful to Michael Floyd (MIT) for discussions on data processing. The authors would like to thank the General Directory of Land Registry and Cadaster (TKGM), the General Command of Mapping (HGK) and TUBITAK MRC Earth and Marine Sciences Institute for giving access to their GNSS data. All seismic data were downloaded from IRIS Data Services.

REFERENCES

Aki, K. 1984. Asperities, barriers, characteristic earthquakes and strong motion prediction, *J. geophys. Res.,* **89**(B7), 5867–5872.

Aksoy, M.E., Meghraoui, M., Vellee, M. & Cakir, Z. 2010. Rupture characteristics of the A.D. 1912 Mürefte (Ganos) earthquake segment of the North Anatolian fault (western Turkey), *Geology,* **38**(11), 991–994.

Ambraseys, N. 2002. The seismic activity of the Marmara sea region over the last 2000 years, *Bull. seism. Soc. Am.,* **92**(1), 1–18.

Ambraseys, N.N. & Jackson, J.A. 2000. Seismicity of the Sea of Marmara (Turkey) since 1500, *Geophys. J. Int.,* **141**(3), F1–F6.

Armijo, R. *et al.*, 2005. Submarine fault scarps in the Sea of Marmara pull-apart (North Anatolian Fault): implications for seismic hazard in Istanbul, *Geochem. Geophys. Geosyst.,* **6**(6), doi:10.1029/2004GC000896.

Bohnhoff, M., Bulut, F., Dresen, G., Malin, P.E., Eken, T. & Aktar, M. 2013. An earthquake gap south of Istanbul, *Nat. Commun.,* **4,** doi:10.1038/ncomms2999.

Bohnhoff, M., Ickrath, M. & Dresen, G. 2016. Seismicity distribution in conjunction with spatiotemporal variations of coseismic slip and postseismic creep along the combined 1999 Izmit–Düzce rupture, *Tectonophysics,* **686,** 132–145.

Bouchon, M. & Karabulut, H. 2008. The aftershock signature of supershear earthquakes, *Science,* **320**(5881), 1323–1325.

Bouchon, M., Bouin, M.P., Karabulut, H., Toksoz, M.N., Dietrich, M. & Rosakis, A.J. 2001. How fast is rupture during an earthquake? New insights from the 1999 Turkey earthquakes, *Geophys. Res. Lett.,* **28**(14), 2723–2726.

Brune, J.N. 1970. Tectonic stress and the spectra of seismic shear waves from earthquakes, *J. geophys. Res.,* **75**(26), 4997–5009.

Cakir, Z., de Chabalier, J.B., Armijo, R., Meyer, B., Barka, A. & Peltzer, G. 2003. Coseismic and early post-seismic slip associated with the 1999 Izmit earthquake (Turkey), from SAR interferometry and tectonic field observations, *Geophys. J. Int.,* **155**(1), 93–110.

Cakir, Z., Ergintav, S., Ozener, H., Dogan, U., Akoglu, A.M., Meghraoui, M. & Reilinger, R. 2012. Onset of aseismic creep on major strike-slip faults, *Geology,* **40**(12), 1115–1118.

Delouis, B., Giardini, D., Lundgren, P. & Salichon, J. 2002. Joint inversion of InSAR, GPS, teleseismic, and strong-motion data for the spatial and temporal distribution of earthquake slip: Application to the 1999 Izmit mainshock, *Bull. seism. Soc. Am.,* **92**(1), 278–299.

Diao, F. *et al.* 2016. Fault locking near Istanbul: indication of earthquake potential from InSAR and GPS observations, *Geophys. J. Int.,* **205**(1), 490–498.

Dreger, D., Nadeau, R.M. & Chung, A. 2007. Repeating earthquake finite source models: strong asperities revealed on the San Andreas Fault, *Geophys. Res. Lett.,* **34**(23), doi:10.1029/2007GL031353.

Dziewonski, A.M., Ekström, G., Woodhouse, J.H. & Zwart, G. 1989. Centroid-moment tensor solutions for July-September 1988, *Phys. Earth planet. Inter.* **56**(3-4), 165–180.

Ekstrom, G., Nettles, M. & Dziewonski, A.M. 2012. The global CMT project 2004–2010: Centroid-moment tensors for 13,017 earthquakes, *Phys. Earth Planet. Int.,* **200–201**(1–9), 1–9. doi:10.1016/j.pepi.2012.1004.1002.

Emre, O., Duman, T.Y., Dogan, A., Ozalp, S., Tokay, F. & Kuscu, I. (2013), *Active Fault Map of Turkey with Explanatory Text Rep.,* General Directorate of Mineral Research and Exploration.

Ergintav, S. *et al.*, 2014. Istanbul's earthquake hot spots: geodetic constraints on strain accumulation along faults in the Marmara seismic gap, *Geophys. Res. Lett.,* **41**(16), 5783–5788.

Evangelidis, C.P. 2015. Imaging supershear rupture for the 2014 M_w6.9 Northern Aegean earthquake by backprojection of strong motion waveforms, *Geophys. Res. Lett.,* **42**(2), 307–315.

Evans, E.L., Loveless, J.P. & Meade, B.J. 2012. Geodetic constraints on San Francisco Bay Area fault slip rates and potential seismogenic asperities on the partially creeping Hayward fault, *J. geophys. Res.,* **117**(B3), doi:10.1029/2011JB008398.

Frank, W.B., Poli, P. & Perfettini, H. 2017. Mapping the rheology of the Central Chile subduction zone with aftershocks, *Geophys. Res. Lett.,* **44**(11), 5374–5382.

Harris, R.A. 2017. Large earthquakes and creeping faults, *Rev. Geophys.,* **55**(1), 169–198.

Herring, T.A., King, R.W. & Floyd, M.A. 2015. *Introduction to GAMIT/GLOBK Introduction to GAMIT/GLOBK Release 10.6,* Massachusetts Institute of Technology.

Hubert-Ferrari, A., Barka, A., Jacques, E., Nalbant, S., Meyer, B., Armijo, R., Tapponnier, P. & King, G. 2000. Seismic hazard in the Marmara Sea region following the 17 August 1999 Izmit earthquake, *Nature,* **404**(6775), 269–273.

Hussain, E., Wright, T.J., Walters, R.J., Bekaert, D., Hooper, A. & Houseman, G.A. 2016. Geodetic observations of postseismic creep in the decade after the 1999 Izmit earthquake, Turkey: implications for a shallow slip deficit, *J. geophys. Res.,* **121**(4), 2980–3001.

Ji, C., Wald, D. & Helmberger, D.V. 2002. Source description of the 1999 Hector Mine, California, earthquake, Part I: Wavelet domain inversion theory and resolution analysis, *Bull. seism. Soc. Am.,* **92**(4), 1192–1207.

Jolivet, R., Simons, M., Agram, P.S., Duputel, Z. & Shen, Z.K. 2015. Aseismic slip and seismogenic coupling along the central San Andreas Fault, *Geophys. Res. Lett.,* **42**(2), 297–306.

Karabulut, H., Roumelioti, Z., Benetatsos, C., Komec Mutlu, A., Ozalaybey, S., Aktar, M. & Kiratzi, A. 2006. A source study of the 6 July 2003 (M_w 5.7) earthquake sequence in the Gulf of Saros (Northern Aegean Sea): seismological evidence for the western continuation of the Ganos fault, *Tectonophysics,* **412**(3–4), 195–216.

Kissling, E., Ellsworth, W.L., Eberhart-Phillips, D. & Kradolfer, U. 1994. Initial reference models in local earthquake tomography, *J. geophys. Res.,* **99**(B10), 19 635–19 646.

Klein, E., Duputel, Z., Masson, F., Yavasoglu, H. & Agram, P. 2017. Aseismic slip and seismogenic coupling in the Marmara Sea: what can we learn from onland geodesy?, *Geophys. Res. Lett.,* **44**(7), 3100–3108.

Konca, A.O. *et al.*, 2008. Partial rupture of a locked patch of the Sumatra megathrust during the 2007 earthquake sequence, *Nature,* **456**(7222), 631–635.

Konca, A.O., Leprince, S., Avouac, J.P. & Helmberger, D. 2010. Rupture Process of M_w 7.1 Duzce earthquake from joint analysis of SPOT, GPS, InSAR, strong-motion, and teleseismic data: a supershear rupture with variable rupture velocity, *Bull. seism. Soc. Am.,* **100**(1), 267–288.

Meade, B.J., Hager, B.H., McClusky, S.C., Reilinger, R.E., Ergintav, S., Lenk, O., Barka, A. & Ozener, H. 2002. Estimates of seismic potential in the Marmara Sea region from block models of secular deformation constrained by Global Positioning System measurements, *Bull. seism. Soc. Am.,* **92**(1), 208–215.

Métois, M., Vigny, C. & Socquet, A. 2016. Interseismic coupling, megathrust earthquakes and seismic swarms along the Chilean Subduction Zone (38°–18°S), *Pure appl. Geophys.,* **173**(5), 1431–1449.

Miyazaki, S., Segall, P., Fukuda, J. & Kato, T. 2004. Space time distribution of afterslip following the 2003 Tokachi-oki earthquake: Implications for variations in fault zone frictional properties, *Geophys. Res. Lett.,* **31**(6), doi:10.1029/2003GL019410.

Nadeau, R.M., Foxall, W. & McEvilly, T.V. 1995. Clustering and periodic recurrence of microearthquakes on the San Andreas Fault at Parkfield, California, *Science,* **267**(5197), 503–507.

Parsons, T. 2004. Recalculated probability of $M \geq 7$ earthquakes beneath the Sea of Marmara, Turkey, *J. geophys. Res.,* **109**(B5), doi:10.1029/2003JB002667.

Perfettini, H. & Avouac, J.P. 2007. Modeling afterslip and aftershocks following the 1992 Landers earthquake, *J. geophys. Res.,* **112**(B7), doi:10.1029/2006JB004399.

Poli, P., Jeria, A.M. & Ruiz, S. 2017. The M_w 8.3 Illapel earthquake (Chile): preseismic and postseismic activity associated with hydrated slab structures, *Bull. geol. Soc. Am.,* **45**(3), 247–250.

Reilinger, R. & et al., 2006. GPS constraints on continental deformation in the Africa–Arabia–Eurasia continental collision zone and implications for the dynamics of plate interactions, *J. geophys. Res.,* **111**(B05411), doi:10.1029/2005JB004051.

Ruiz, S. *et al.* 2016. The seismic sequence of the 16 September 2015 M_w 8.3 Illapel, Chile, *Earthquake,* **87**(4), doi:10.1785/0220150281.

Saltogianni, V., Gianniou, M., Taymaz, T., Yolsal-Çevikbilen, S. & Stiros, S. 2015. Fault slip source models for the 2014 M_w 6.9 Samothraki-Gökçeada earthquake (North Aegean Trough) combining geodetic and seismological observations, *J. geophys. Res.,* **120**(12), 8610–8622.

Schmittbuhl, J., Karabulut, H., Lengline, O. & Bouchon, O. 2016. Seismicity distribution and locking depth along the Main Marmara Fault, Turkey, *Geochem. Geophys. Geosyst.,* **17**(3), 954–965.

Schmittbuhl, J., Karabulut, H., Lengliné, O. & Bouchon, M. 2016. Long-lasting seismic repeaters in the Central Basin of the Main Marmara Fault, *Geophys. Res. Lett.,* **43**(18), 9527–9534.

Shirzaei, M. & Bürgmann, R. 2013. Time-dependent model of creep on the Hayward fault from joint inversion of 18 years of InSAR and surface creep data, *J. geophys. Res.,* **118**(4), 1733–1746.

Stein, R., Barka, A. & Dieterich, J. 1997. Progressive failure on the North Anatolian fault since 1939 by earthquake stress triggering, *Geophys. J. Int.,* **128**(3), 594–604.

Taymaz, T., Jackson, J. & McKenzie, D. 1991. Active tectonics of the north and central Aegean Sea, *Geophys. J. Int.,* **106**(2), 433–490.

Vernant, P., Reilinger, R. & McClusky, S. 2014. Geodetic evidence for low coupling on the Hellenic subduction plate interface, *Earth planet. Sci. Lett.,* **385,** 122–129.

Waldhauser, F. (2001), HypoDD: A computer program to compute double-difference earthquake locations, U. S. Geol. Surv. Open-File Rep., 01–113.

Waldhauser, F. & Ellsworth, W.L. 2000. A double-difference earthquake location algorithm: Method and application to the northern Hayward fault, California, *Bull. seism. Soc. Am.,* **90**(6), 1353–1368.

Waldhauser, F. & Ellsworth, W.L. 2002. Fault structure and mechanics of the Hayward Fault, California, from double-difference earthquake locations, *J. geophys. Res.,* **107**(B3), ESE 3-1–ESE 3-15.

Wells, D.L. & Coppersmith, K.J. 1994. New empirical relationships among magnitude, rupture length, rupture width, rupture area, and surface displacement, *Bull. seism. Soc. Am.,* **84**(4), 974–1002.

Yamanaka, Y. & Kikuchi, M. 2004. Asperity map along the subduction zone in northeastern Japan inferred from regional seismic data, *J. geophys. Res.,* **109**(B7), doi:10.1029/2003JB002683.

Yue, H., Lay, T., Schwartz, S.Y., Rivera, L., Protti, M., Dixon, T.H., Owen, S. & Newman, A.V. 2013. The 5 September 2012 Nicoya, Costa Rica M_w7.6 earthquake rupture process from joint inversion of high-rate GPS, strong-motion, and teleseismic *P* wave data and its relationship to adjacent plate boundary interface properties, *J. geophys. Res.,* **118**(10), 5453–5466.

SUPPORTING INFORMATION

Supplementary data are available at *GJI* online.

Figure S1. Map of stations used for relocation of earthquakes from BDTIM, AFAD and NOA networks.

Figure S2. Statistics for the (a) longitude (b) latitude and (c) depth errors for the seismic activity before the 2014 main shock, between 2007 June 1 and 2015 May 23. (d) Earthquake magnitude and total number of earthquakes and best fitting *b*-value for the Gutenberg–Richter relationship.

Figure S3. Statistics for the (a) longitude (b) latitude and (c) depth errors for the aftershocks of M_W6.9 North Aegean earthquake, between 2014 May 24 and 2015 August 23. (d) Earthquake magnitude distribution and the best fitting *b*-value for the Gutenberg–Richter relationship.

Figure S4. Relative longitude, latitude and depth errors after double-difference relocation.

Figure S5. Time-series from daily position estimates of the cGPS sites which are located in Turkey (ATHT, CANA, TYF1) and in Greece (LEMN). The jump on 144 GPS day results from M_w6.9 earthquake on 24 May 2014. The error bar represents formal 1σ standard deviations.

Figure S6. Observed (black) and synthetic (red) teleseismic *P* and *SH* waveforms. Station name, azimuth and distance are indicated on the left of each trace. The maximum displacement is shown at the top right of each trace in microns.

Figure S7. Comparison of input models with the output models for the two resolution tests performed, using the GPS data only.

Figure S8. Slip models with different smoothness constraints. For each model associated misfits are tabulated to the right of he slip map.Variance reduction for the *P* and *SH* waveforms are calculated as $\mathrm{VR} = 100 \times [1 - \frac{\sum_{i=1}^{n} (d^i - s^i)^2}{\sum_{i=1}^{n} (d^i)^2}]$. For the GPS displacement vectors, the reduced χ^2 is calculated by $\chi_r^2 = \frac{1}{n} \sum_{i=1}^{i=n} (\frac{\mathrm{pred}^i - \mathrm{obs}^i}{\sigma^i})^2$.

Figure S9. Time evolution of spatial distribution of aftershocks projected on the fault plane with coseismic slip distribution for the joint geodetic and teleseismic model.

Table S1A. Survey GPS sites derived coseismic displacements.

Table S1B. cGPS stations derived coseismic displacements.

Table S1C. GPS-reported coseismic displacements in Greece (from Saltogianni *et al.* 2015).

Please note: Oxford University Press is not responsible for the content or functionality of any supporting materials supplied by the authors. Any queries (other than missing material) should be directed to the corresponding author for the paper.